1 **Water vapor induced self-assembly of islands/honeycomb structure by secondary phase**

2 **separation in polystyrene solution with bimodal molecular weight distribution**

3 Authors: Maciej Łojkowski[1,*], Adrian Chlanda[1,2], Emilia Choińska[1], Wojciech

4 Swieszkowski[1*].

5 Affiliation:

6 1. Faculty of Material Sciences and Engineering, Warsaw University of Technology,

7 Wołoska 141, 02-507 Warsaw, Poland

8 2. Department of Chemical Synthesis and Flake Graphene, Łukasiewicz Research

9 Network - Institute of Microelectronics and Photonics, Aleja Lotników 32/46, 02-

10 668 Warsaw, Poland.

11 **Abstract**

12 The formation of complex structures in thin films is of interest in many fields. Segregation of

13 polymer chains of different molecular weights is a well-known process. However, here,

14 polystyrene with bimodal molecular weight distribution, but no additional chemical

15 modification was used. It was proven that at certain conditions, the phase separation occurred

16 between two fractions of bimodal polystyrene/methyl ethyl ketone solution. The films were

17 prepared by spin-coating, and the segregation between polystyrene phases was investigated by

18 force spectroscopy. Next, water vapour induced secondary phase separation was investigated.

19 The introduction of moist airflow induced the self-assembly of the lower molecular weight into

20 islands and the heavier fraction into a honeycomb. As a result, an easy, fast, and effective

21 method of obtaining island/honeycomb morphologies was demonstrated. The possible

22 mechanisms of the formation of such structures were discussed.

23

24 **Keywords**

25 self-assembly; polymer thin films; bimodal molecular weight distribution; polystyrene; spin-

26 coating; honeycomb; breath figures; liquid-liquid phase separation; viscoelastic phase

27 separation; secondary quench;

28

29 **Introduction**

30 Complex morphologies compromising micro-islands and especially micropillars have gained

31 attention due to their wide range of possible applications, such as their special wetting

32 properties (1,2), application in studying biofilm formation (3), or controlling stem cell

33 differentiation (4). Two widespread methods that allow the creation of a broad range of

34 structures of polymer thin films (PTFs) are spin-coating (5) and breath figures (6). These

35 methods were applied for manufacturing organic ferroelectric switches (7), light-emitting

36 devices (8), sensors (9,10), drug delivery systems (11,12), biologically active surfaces (13,14),

37 functional nanostructured surfaces (15,16), and membranes (17). These processes rely heavily

38 on the interaction dynamics between the solvent, the polymer, and the vapours in the vicinity

39 of the surface. During spin-coating, a droplet of a mixture of a solvent and one or two polymers

40 is dropped onto the substrate. Subsequently, the substrate is rotated very quickly to cover it

41 uniformly with the solution's liquid film. As a result, the solvent evaporates. Thus, solvent and

42 temperature quench occurs. The spin coating can be divided into time regions. First, the liquid

43 solution droplet is spread hydrodynamically over the substrate. This regime is often referred to

44 as hydrodynamic thinning. Later, when a flat layer of the solution was obtained, the evaporation

45 of the solvent was responsible for further thinning of this layer.(18) Changes in the solvent

46 volume fraction and temperature often lead to unintentional or intentional liquid-liquid phase

47 separation.(19) It has been argued that such phase separation often starts in the early stages of

48 the regime controlled by evaporation.(19,20) Further spinning of the solution leads to gel

49 formation, which eventually slows down the diffusion inside the film. As a result, the

50   morphology becomes frozen in time before reaching equilibrium. The time necessary for the

51   morphology to stop evolving depended on the solvent evaporation rate, solution viscosity,

52   spinning rate, and substrate thermal properties.(21–23) During coating formation, a range of

53   events attributed to the local thermal instabilities takes place: heat transfer between the bottom

54   and top layers of the film; heat transfer from the air above the layer; heating the substrate by

55   the surrounding air; and local lateral temperature variance due to the thermal conductivity and

56   heat capacity of the substrate.(23) These events may lead to the unnecessary or intended

57   waviness of the coating profile. This undulation is often attributed to two interconnected

58   phenomena. One is the flow of the liquid due to thermal convection. The second is the surface

59   tension gradient due to local composition differences, which manifests in solvent-rich or

60   solvent-depleted areas.(18) The solvent-depleted areas have higher surface tension and thus

61   pull the liquid towards these areas and up, while the solvent-rich areas sink, forming valleys.

62   High centrifugal force during spin-coating is often a cause of elongation of the mentioned

63   structures. As a result, long stripes extending from the centre of the sample are observed. Using

64   solvents with low surface tension, the addition of a surfactant or using a mixture of solvents

65   can suppress the formation of these features. Furthermore, decreasing the amount of heat can

66   suppress the formation of convection cells and allow smooth coating preparation.

67   In the second technique mentioned above, breath figures appear on the liquid film's surface

68   when the humid airflow accelerates the evaporation rate. Successively, the temperature

69   decreases, which results in nucleation and growth of water droplets. These droplets create a

70   regular honeycomb array of cavities in the film. The temperature increased to that of the

71   surroundings, and the droplets evaporated, leaving a porous surface. After most of the solvent

72   had evaporated, the start of droplet nucleation was governed by the onset time related to the

73   solvent evaporation rate, solution concentration, and airflow.(24)

74 The location and width of the MWD can affect solid thin polymeric film formation to achieve

75 unique properties (25). Wu et al. studied the effect of MWD on the self-assembly of end-

76 functionalized polystyrenes. They proposed a new way of controlling the morphology of PTF

77 obtained via breath figures by changing the MWD width. As a result, a porous membrane with

78 higher robustness was obtained.(26) The width of the MWD can be tailored either within the

79 polymerization process (27,28) or by mixing two polymer species with a very narrow MWD

80 (29). Heitmiller et al. reported that a heterogeneous melt of polyethylene had a higher flow

81 index than a homogeneous melt.(30) The investigation performed by Koningsveld et al. has

82 shown that the bimodal MWD has a significant effect on the liquid-liquid binodal curve of

83 polymers in solution.(31) Phase regions characterise such solutions, and liquid-liquid phase

84 separation between polymer- and solvent-rich fractions can occur. Zeman et al. demonstrated

85 that the critical concentration enabling phase separation in a solution of two polymer species

86 decreases with an increase in the molecular weight M_w.(32) Moreover, even when the polymer-

87 polymer interactions are athermal, i.e. Flory-Huggins interaction parameter χ equals zero, and

88 phase separation can occur due to the large difference in entropy between long and short chains,

89 which act as separate entities and influence the viscosity of bimodal solutions.(33) The

90 evaporation of the solvent followed by temperature quenching can be responsible for phase

91 separation, as the Flory-Huggins parameter is temperature dependent and decreases with

92 temperature. The quenched mixture can turn from the one-phase state to an unstable state.

93 Interestingly, Henderson et al. investigated a two-step process in which the first temperature

94 quench forces phase separation and the spinodal structures are allowed to coarsen; next, even

95 deeper quenching is enacted.(34) This two-step quench led to the formation of small well-

96 dispersed domains within the primary domains. Intriguingly, the combined spin-coating and

97 breath figure methods would lead to two quenching and heating events. First, solvent

98 evaporation would decrease the temperature. Second, water condensation would increase the

temperature, and finally, evaporating water would again decrease the temperature. Another interesting theory is "viscoelastic phase separation". Phase separation occurs due to an imbalance of the viscoelastic properties of the components.(35) Polymer melts with bimodal molecular weights show nonlinear rheology. A rheological investigation by Hengeller et al. reported two regimes of stress relaxation in such a melt, where either the only short or only long chains underwent stress relaxation, depending on the time scale.(36) Harris et al. found that the viscosity of the blend of bimodal polystyrene can be considered a sum of components.(37) It has been discussed that blending polystyrenes with different molecular weights mixed the entanglement types between polymer chains. The polymer concentration in the solvent changes how the polymer chains interact. Two polymer chains act as separate entities, provided that the concentration is below the overlap concentration (C*). However, once the overlap concentration occurs, the polymer's cooperative motion starts, and the behaviour of the solution changes.(38,39)

Successive research has focused on studying how polymer chains of varying lengths segregate in PTFs. Hariharan et al. investigated the effect of the entropy of spin-coated and annealed bimodal PTFs on polymer chain segregation.(40) It was shown that higher entropy of shorter chains led to their segregation on the PTF surface, while the longer chains' lower entropy promoted their segregation in bulk. Tanaka et al., in turn, studied spin-coated polystyrene blends with low and high M_w with narrow MWD utilizing toluene as a solvent. They reported that PTFs consisting of polystyrenes with a low molecular weight demonstrated surface segregation after thermal treatment.(29) Several other recent studies have illustrated the segregation of lower molecular mass elements towards the surface during annealing.(41–45) On the other hand, it has been shown that deuterated polymer segregation can change the surface roughness after annealing the coating.(46–49)

123 In the present study, to modify the coating morphology, we decided to explore the phase

124 separation between two kinds of polystyrene with low and high molecular weights mixed in a

125 solvent. We changed the polydispersity, and we used uniform polystyrene standards as a

126 reference. The solvent methyl ethyl ketone MEK was chosen because of its suitability for spin-

127 coating.(50) However, for most, its hygroscopic properties, as we planned to perform spin-

128 coating in humid conditions. MEK is considered a marginal solvent for PS, while it is more

129 hygroscopic than typically used solvents for polystyrene.(51,52)

130 For our study, we established the following assumptions. The mixture with sufficiently high

131 polydispersity will phase separate during spin-coating, even if these species are chemically

132 identical. The study will be performed in the regime where thermocapillary effects cause

133 undulations to make any morphological changes clearer to observe. The breath figure technique

134 will be combined with spin-coating to induce additional motion caused by the surface tension

135 of water.

136 The study is organized in the following order. First, the effect of the bimodal weight distribution

137 on the viscosity of the solutions is discussed. Next, the morphology of the coatings spun at the

138 most negligible possible humidity is compared by analysis of atomic force microscopy and

139 optical microscopy images. Then, force spectroscopy was used to identify the different

140 polystyrene phases. In situ reflectometry was used to measure the evaporation time of the

141 solutions. Finally, the coatings spun at different humidity levels were investigated by optical

142 and atomic force microscopy.

143 It was found that at a relative humidity of 75%, a solution concentration of 80 mg/ml and

144 polystyrene molecular weights of 20 kDa and 200 kDa mixed in a 75/25 w/w% ratio, the two

145 phases formed islands (lower M_w fraction) embedded inside of the honeycomb (higher M_w

146 fraction).

147 Although spin-coating was chosen for its ease of controlling the evaporation rate, we believe

148 that the proposed method can be extended to other techniques, such as dip-coating or ink-jet

149 printing. The presented results can also be treated as a starting point for other interesting

150 experiments.

151

152 **Result and discussion**

153 The solutions with bimodal MWD were prepared so that the two nodes in the distribution were

154 clearly separated. The GPC molecular weight distribution of a single node MWD (uniform) is

155 presented in Fig. 1 A, which illustrates the MWD of 91 kDa polystyrene with a narrow

156 distribution (PDI=1.04). In contrast, Fig. 1 B illustrates the MWD with two nodes of a blend of

157 91 kDa PS with 200 kDa PS, both with narrow distributions (PDI=1.04).
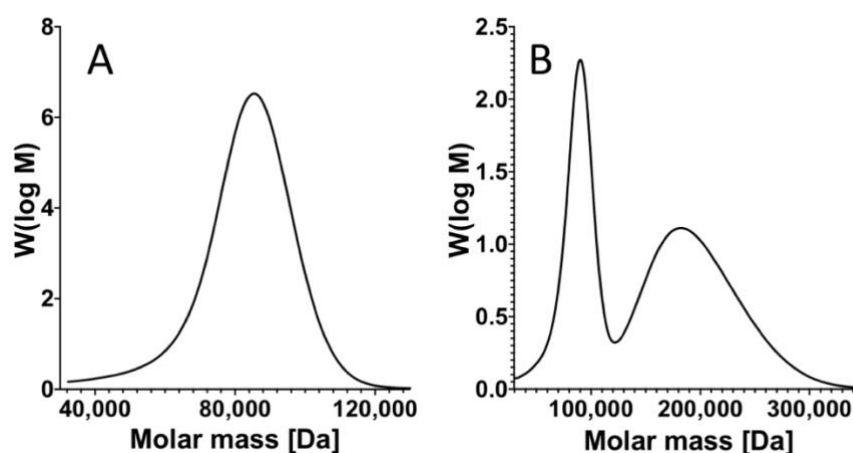
158

159

160 Fig 1. Exemplary GPC experiment results of bimodal and uniform MWD polystyrene; A -

161 narrow uniform MWD, Mw = 91 kDa, PDI 1.04; B – bimodal MWD, blend of Mw = 91 kDa,

162 PDI = 1.04 and Mw = 200 kDa, PDI = 1.04. (GraphPad Prism 9, https://www.graphpad.com)

163

164 • **Evaluation of solution viscosities**

165 The viscosity measurement (Fig. 2) can be used to assess not only the final coating thickness

166 and the solvent evaporation time prediction but also the characteristics of polymer chain

167   interactions. The measurement result is presented as reduced viscosity η_r/C, where C represents

168   the concentration in mg/ml. Here, $\eta_r = \frac{\eta - \eta_s}{\eta_s}$, where η is the dynamic viscosity of the solution

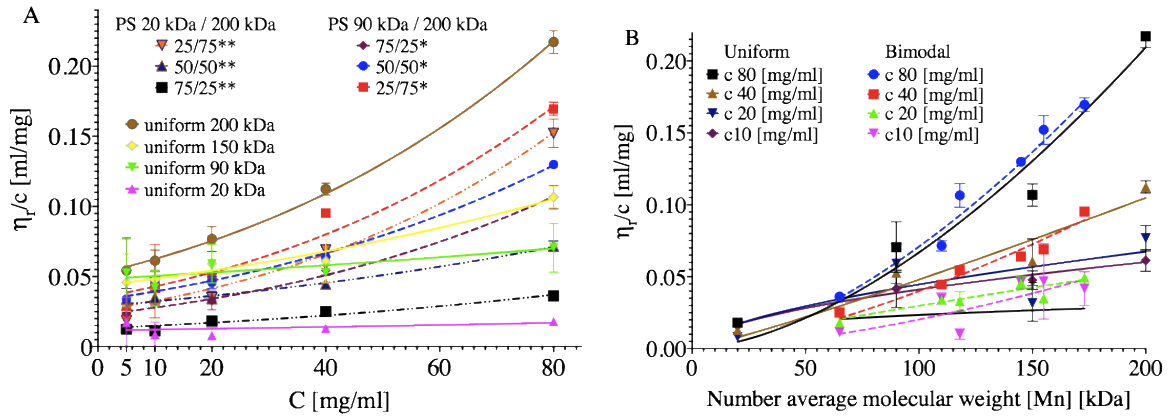169   and η_s is the viscosity of the solvent. In Fig. 2A, the viscosity is plotted as a function of the

170   concentration.

171

172

173   Fig. 2. Reduced viscosity η_r/C of the solutions, A - η_r/C plotted against the solution's

174   concentration. Curves represent fits for eq. 2; B - η_r/C plotted as a function of the number

175   average molecular weight function. Curves represent the Mark-Houwink equation fit (eq. 3),

176   $[M_n] = f_1 M_{w1} + f_2 M_{w2}$, where f is w/w % ratio of polymers. (GraphPad Prism 9,

177   https://www.graphpad.com)

178

179   The general dependence of viscosity on concentration can be described in the form of a power

180   series:(53)

181   $\frac{\eta_r}{C} = [\eta](1 + K[\eta]C + \frac{K[\eta]C^2}{2} + \frac{K[\eta]C^3}{6})$ (2)

182   where $[\eta]$ is the intrinsic viscosity at infinite dilution. The coefficients are summarised in Table

183   S1 in SI. The intrinsic viscosity $[\eta]$ was lower for bimodal blends. The overlap concertation is

184   defined as the concentration at which the polymer chains start to overlap with each other.(54)

185   The overlap concertation was estimated according to C*=1/$[\eta]$. The overlap concentration for

186 20 kDa was 83 mg/ml and for 200 kDa was 19 mg/ml. Notably, in the case of the 80 mg/ml

187 solution, the 20 kDa species were in the semidilute regime, while the 200 kDa species were in

188 the concentrated regime.

189 The viscosity of the bimodal solutions increased faster with increasing concentration than in

190 the case of uniform solutions. The K parameter was particularly high for 75/25 blends: 1.36 for

191 90 kDa and 200 kDa and 1.01 for 20 kDa and 200 kDa. In comparison, K for uniform 200 kDa

192 was 0.36. Thus, it can be assumed that the number of entanglements attributed to the 200 kDa

193 fraction rises at higher concentrations. Fig. 2B presents the viscosity in relation to the number

194 molecular weight [M_n]. The relation between viscosity and molecular weight can be described

195 in the form of the Mark-Houwink equation:(53)

196 $$\frac{\eta_r}{c} = \ln K + a\ln[M_n]. \tag{3}$$

197 The K and [η] values are summarised in SI, Table S2. The uniform solutions were visibly more

198 viscous than their bimodal counterparts of similar molecular weights at concentrations below

199 20 mg/ml. It could be expected that the bimodal solutions will change their behaviour more

200 severely when solvent evaporation would quench them towards more concentrated regimes.

201

202 • **Evaporation of the solvent during spin-coating**

203 As presented in Fig. 3, the evaporation rate R depends on the viscosity of the solutions. The

204 evaporation of the 20 kDa, 91 kDa and 200 kDa samples differs for the same concentration.

205 These differences became more transparent at a concentration of 80 mg/ml.
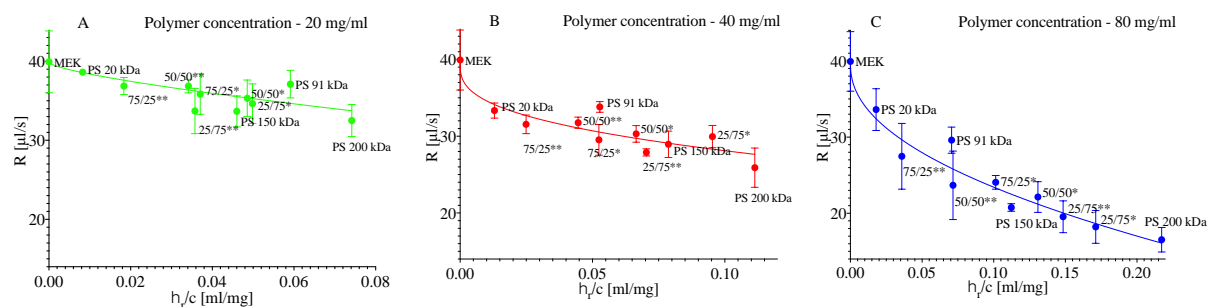
206

Fig. 3. The relation between the evaporation rate of solution and the reduced viscosity of solution for polymer concentrations: A - 20 mg/ml, B - 40 mg/ml, and C - 80 mg/ml. The curves represent the Padé approximation trend line. (GraphPad Prism 9, https://www.graphpad.com)

- **Investigation of the thickness and morphology of the coatings spun at a relative humidity of 0%**

The coatings spun at Rh 0% were chosen as a starting point for the investigation. We decided to look for phase separation if no humidity was applied, affecting the investigated solvent-polymer system. The convection Marangoni flow, solvent evaporation, and phase separation events alter the coating surface morphology. As a result, the occurrence of wrinkles or arrays of islands on the coating surface was reported. (48,55–57)

The coatings were investigated via AFM and optical imaging to determine the effect of bimodal MWD on coating morphology. Significant differences between blend types occurred (Fig. 4A). The solution concentration of 80 mg/ml was chosen. As we expected from the tests mentioned earlier, the bimodal distribution role would be the highest. Moreover, we wanted to avoid the influence of the substrate on our force spectroscopy experiment. For that, we needed the thickest coating. As illustrated in Fig. 4B, the thickness of the coatings in the case of 80 mg/ml scaled linearly with the blends' average molecular weight. No correlation between the thickness and roughness was found. (Fig. 4C).
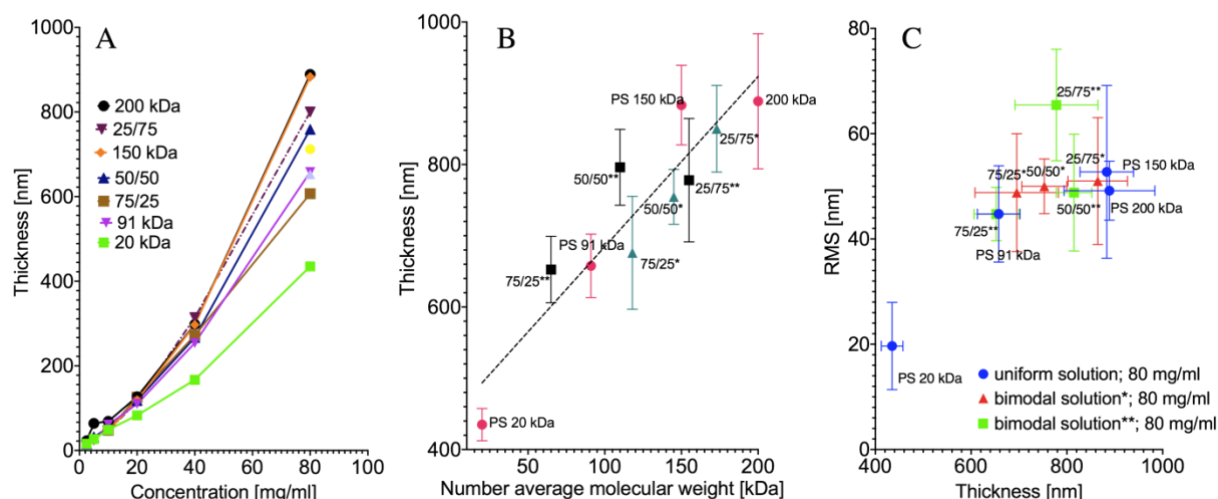
Fig. 4. A - Thickness of the coatings with respect to the composition and the concentration. The plot presents data for uniform and 91 kDa/200 kDa solutions. B – Thickness of the coating for 80 mg/ml concentration in the blend's molecular weight function. * - Blends of 91 kDa and 200 kDa polystyrene; ** - blend of 20 kDa and 200 kDa polystyrene; x/x – w/w% ratio of blended homogeneous polystyrenes. The number average molecular weight $[M_n] = f_1 M_{w1} + f_2 M_{w2}$, where f w/w. % ratio of polymers. C - RMS roughness of the coatings spun from 80 mg/ml concentration. (GraphPad Prism 9, https://www.graphpad.com)

To represent the morphology of the material quantitatively, one can apply the Minkowski parameters.(58) The images (Fig. 5A) used for analysis come from the central part of the image to exclude the high shear rate effect on the coating morphology. The scale bar was 50 μm. Based on this description, it can be concluded that the morphology of the uniform coatings is characterised by separate islands surrounded by a bicontinuous phase. In contrast, the bimodal coatings are characterised by a bicontinuous phase separated by interconnected islands.

Fig. 5B presents connectivity. Connectivity $C(\nu)$ can be used to describe the bicontinuous or island morphology of the coating with respect to the given binarization threshold ν. A negative value of connectivity corresponds to bicontinuous morphology, while a positive value corresponds to island morphology. The threshold was normalized to 1. Based on the

247 connectivity, the bimodal coatings had different morphologies than the uniform coatings when

248 the starting conditions (Rh 0%) were considered. With the exclusion of the 75/25 20 kDa 200

249 kDa coating, the coatings were characterized by peaks related to continuous structures and two

250 peaks related to islands.

251 In contrast, the uniform coatings had one set of continuous structures and two peaks related to

252 islands. In connection with the images, it can be assumed that these two kinds of islands are

253 one on top of another. In the case of bimodal blends, the presented situation describes a set of

254 interconnected islands on top of another interconnected structure.
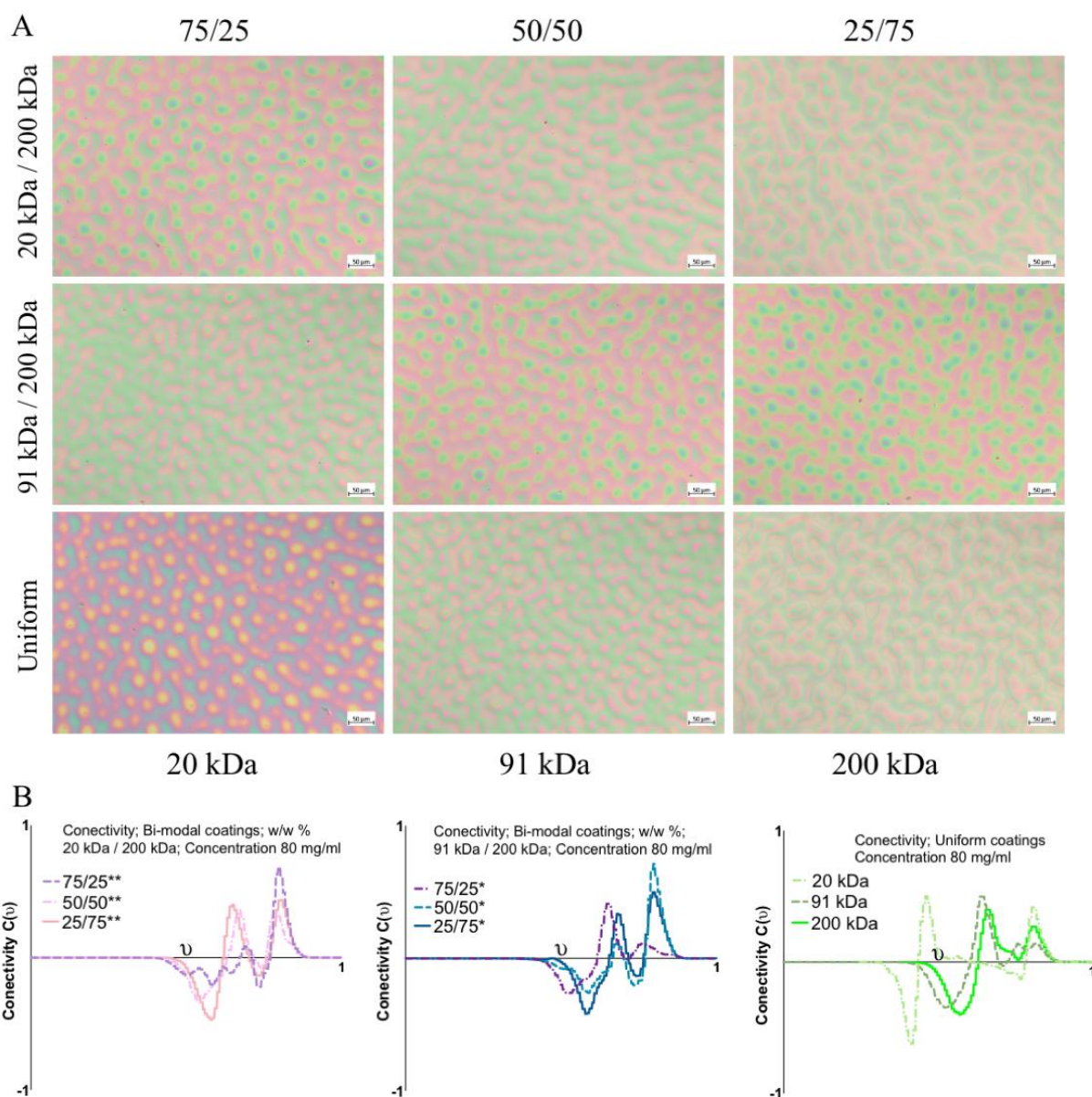
255

Fig. 5. A - Optical images of coatings spun from 80 mg/ml. The B - Minkowski connectivity $C(\nu)$ of the coatings spun from 80 mg/ml, where ν represents the threshold for image binarization. The values on the axis were normalized to 1. (PowerPoint 365, GraphPad Prism 9, https://www.graphpad.com)

- **Investigation of coating phase composition by means of AFM force spectroscopy**

The AFM force spectroscopy method allows the visualization and quantification of surface areas differing in mechanical properties.(59) The coatings spun from the solutions with 80

265 mg/ml concentration were studied. The resulting elastic modulus of the coatings was calculated
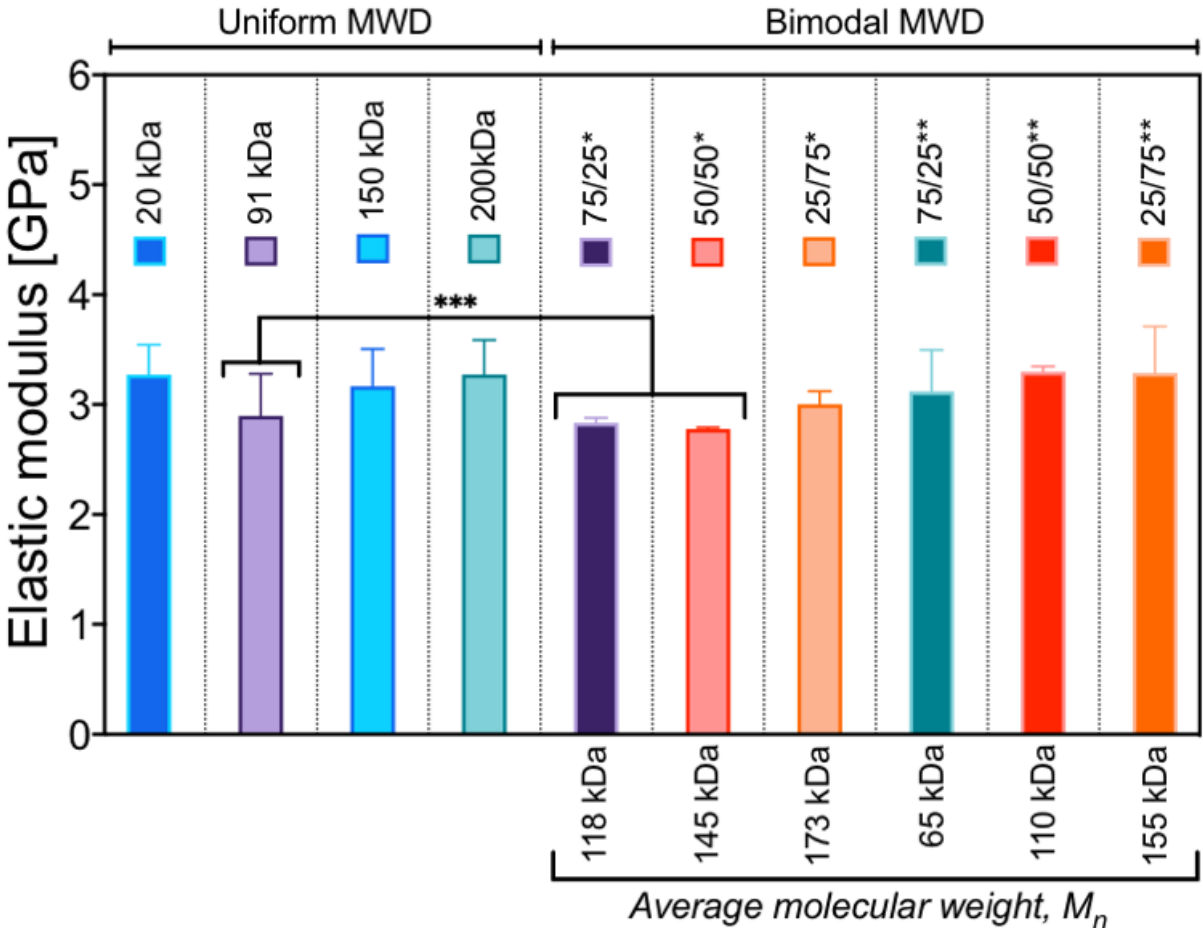
266 (Fig. 6).

267

268

269 Fig. 6. Average elastic modulus obtained based on the FS method for coatings made from a

270 solution of 80 mg/ml. Uniform – coatings were made from homogeneous solutions; bimodal –

271 coatings made from solutions with bimodal MWD; * - blends of 91 kDa and 200 kDa

272 polystyrene; ** - blend of 20 kDa and 200 kDa polystyrene; x/x – w/w% ratio of blended

273 homogeneous polystyrenes. $[M_n] = f_1 M_{w1} + f_2 M_{w2}$, where f w/w % ratio of polymers. *** -

274 means are significantly different (one-way ANOVA, $p < 0.05$). (GraphPad Prism 9,

275 https://www.graphpad.com)

276

277   The obtained results are similar to those found in the literature.(60) The uniform 91 kDa coating

278   and the 75/25 and 50/50 blends of 91 kDa and 200 kDa had significantly lower elastic moduli

279   than the rest of the tested groups. The dependence between the molecular weight and the elastic

280   modulus of the polymer has been repeatedly proven.(61,62) However, we did not find

281   significant differences between the other groups. The uniform 20 kDa coating had an elastic

282   modulus similar to that of the 200 kDa coating in our investigation. The 20 kDa coating was

283   the thinnest; thus, the substrate could influence the result. We performed a linear regression test

284   (SI, *Force Spectroscopy*, Fig. S4) between the thickness of the 80 mg/ml coatings and the elastic

285   modulus, which proved no relationship between the thickness of the coatings and the elastic

286   modulus, while the 20 kDa coating was an outlier (SI, *Force Spectroscopy*, Table S14).
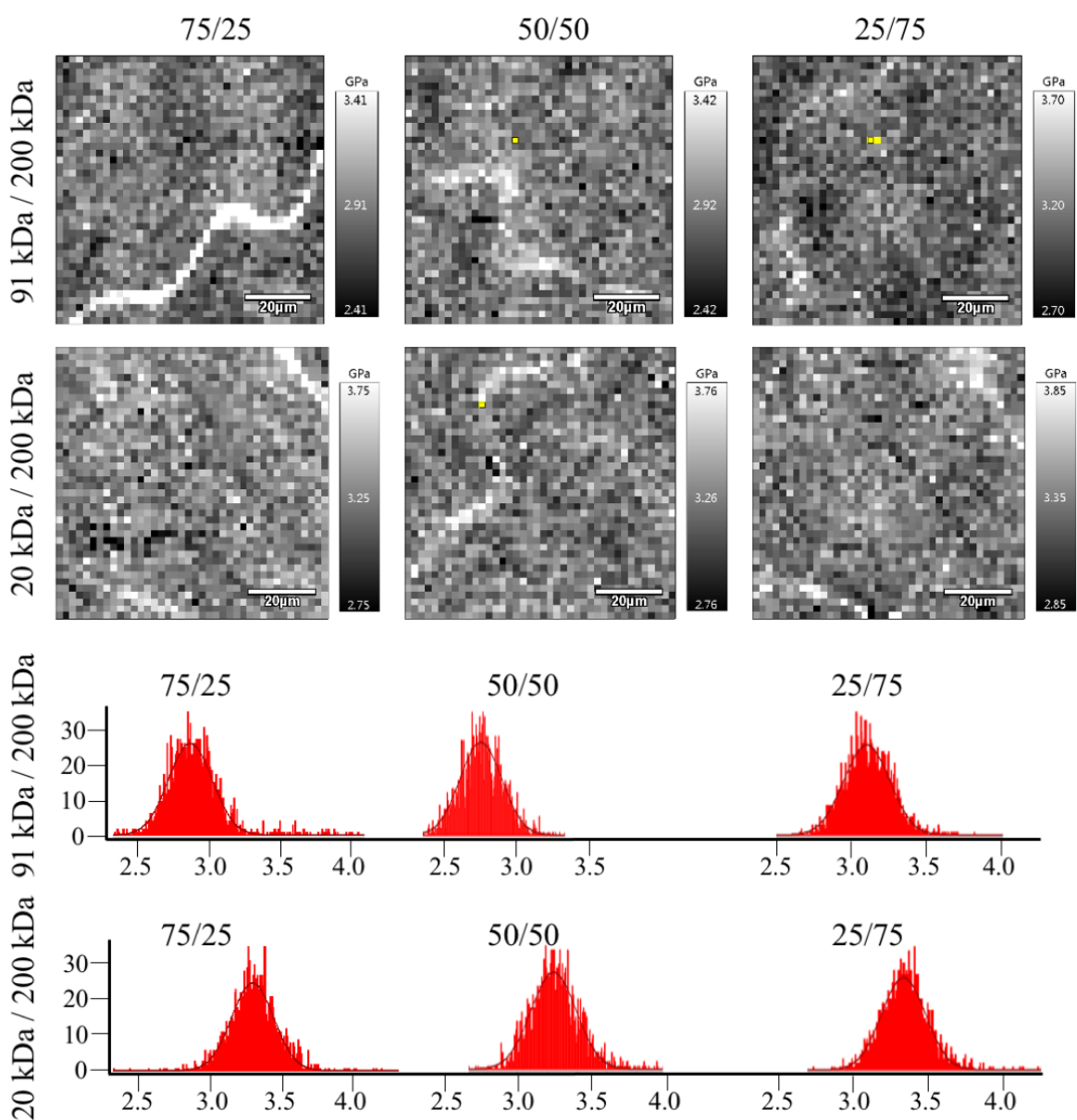
Fig. 7. Force spectroscopy maps of bimodal MWD coatings and corresponding histograms of the elastic modulus. The greyscale shows the stiffness – the white colour corresponds to the highest stiffness. The grayscale range is ± 1 GPa. (PowerPoint 365, Igor Pro 6.37 with Asylum Research 15.02.105 add-on, https://afm.oxinst.com)

Interestingly, it was possible to record local differences in the coating surface stiffness (Fig. 7). The maps were gathered for bimodal coatings. White spinodal-like areas are characterized by

higher stiffness. The differences are more clearly visible in the case of 90 kDa and 200 kDa

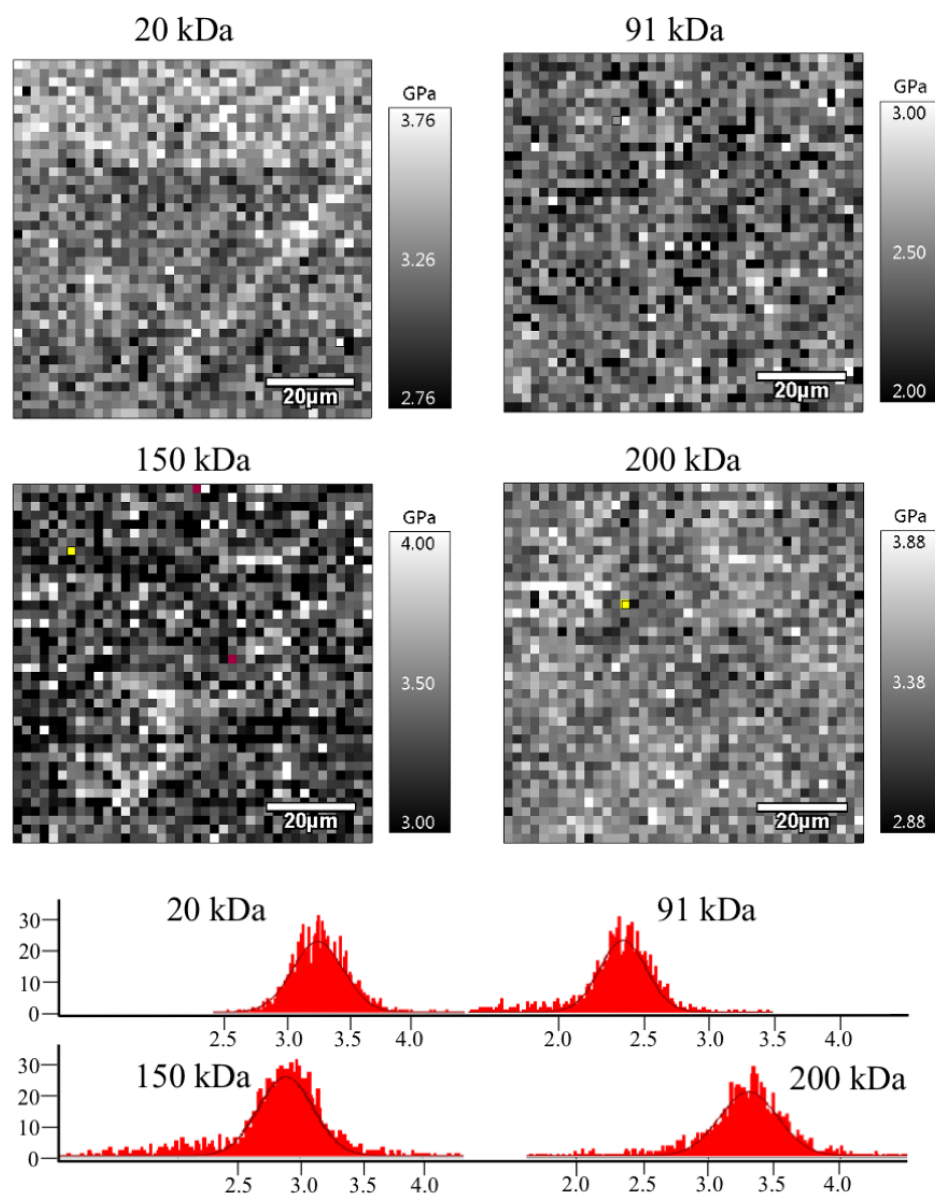blends, in agreement with Fig. 6.

Fig. 8. Force spectroscopy maps of coatings with uniform MWD and corresponding histograms

of the elastic modulus. The greyscale shows the stiffness – the white colour corresponds to the

highest stiffness. The grayscale range is ± 1 GPa. (PowerPoint 365, Igor Pro 6.37 with Asylum

Research 15.02.105 add-on, https://afm.oxinst.com)

304 For comparison, Fig. 8 illustrates the FS maps of the uniform coatings. We analysed the

305 skewness of the maps' elastic modulus distribution (SI, *Force Spectroscopy*, Table S15). The

306 skewness in the case of uniform coatings was significantly lower ($p < 0.05$) than that in the case

307 of bimodal coatings (Fig. 9). The distribution of the elastic modulus of the uniform coatings
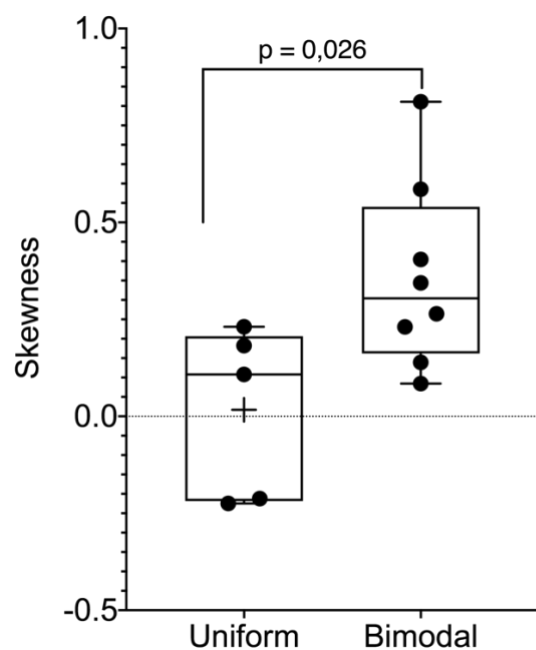
308 was more homogeneous.

309
310 Fig 9. The skewness of the elastic modulus data sets. Uniform – grouped means that represents

311 the skewness of histograms of uniform coatings elastic modulus. Bimodal – grouped means that

312 represents the skewness of histograms of all kinds of bimodal blends elastic modulus. The

313 means of these two groups were significantly different ($p < 0.05$). (GraphPad Prism 9,

314 https://www.graphpad.com)

315

316 Therefore, it was concluded that force spectroscopy revealed phase separation in the bimodal

317 coatings. The most noteworthy phase separation was found for the 75/25 blends of both kinds

318 of bimodal coatings. Here, the phase of lower concentration formed long, spinodal-like forms.

319 For the 25/75 blends, the separate phases were scattered.

320

321 • **Solubility of polystyrenes with respect to the molecular weight distribution**

322 The phase separation mentioned above could be explained by solubility investigation. It was

323 shown that the viscosity of the polymeric solution could be utilised by the application of the

324 Mangaraj method to retract several polymer-solvent parameters, i.e. the Flory interaction

325 parameter.(63) We utilised the Mangaraj equation (eq. 4) to investigate the miscibility gap

326 between the lower- and higher-molecular-weight polystyrenes.(64)

327 $$\ln\left(\frac{\eta}{\eta_{max}}\right) = -(\delta_s - \delta_{eff})^2. \tag{4}$$

328 The effective miscibility parameter δ_{eff} was calculated with respect to a solution of 200 kDa

329 with a concentration of 80 mg/ml, which had the highest viscosity among the tested solutions

330 (η_{max}). The solvent δ_s was set to 19 MPa$^{0.5}$, which is a typical value for MEK.

331 The miscibility gap between low- and high-molecular-weight polystyrene can be derived based

332 on the PS blends' viscosity. Furthermore, the miscibility gap decreases accordingly with the

333 low molecular weight fraction. Here, δ_{eff} is the effective Hildebrand miscibility parameter

334 calculated based on the intrinsic viscosity *[η]*. For the 20 mg/ml concentration, all the solutions

335 are present on the same linear trend with the lowest δ_{eff} for the highest molecular weight. It

336 should be noted that with increasing concentration, the trends for 20 kDa/200 kDa solutions

337 (brown squares), 91 kDa/200 kDa solutions (purple triangles), and uniform solutions (blue

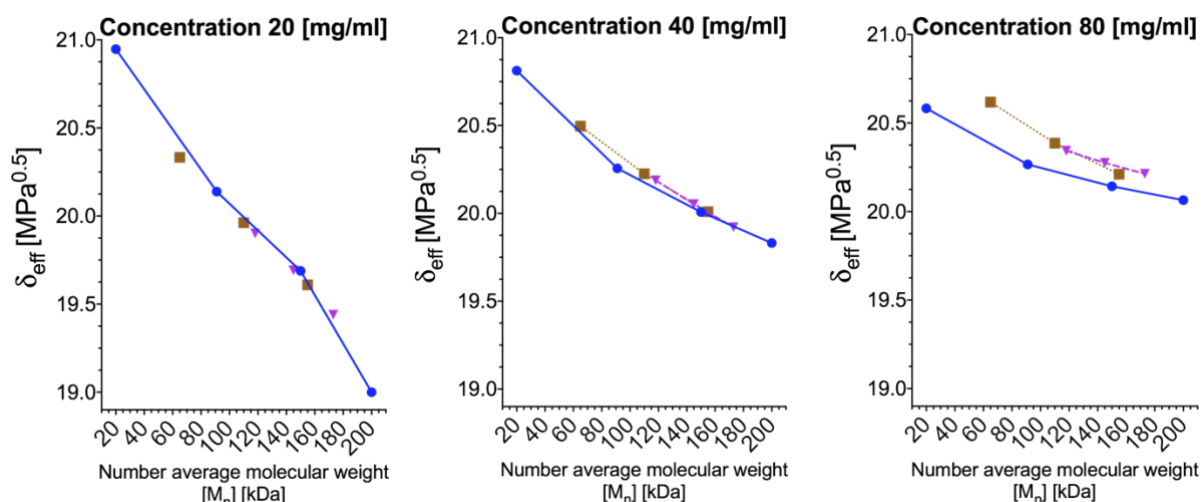338 circles) become divergent at low molecular weights, with their trends coincident at 200 kDa

339 (Fig. 10).

340

Fig. 10. The effective miscibility parameter δ_{eff} of the polystyrenes in MEK with bimodal and uniform distributions for two kinds of bimodal distributions: 20 kDa/200 kDa – brown squares and 91 kDa/200 kDa – purple triangles; the blue circles represent data for polystyrenes with uniform distributions. $[M_n] = f_1 M_{w1} + f_2 M_{w2}$, where f w/w % ratio of polymers. (GraphPad Prism 9, https://www.graphpad.com)

- **Self-assembly of micro islands/honeycombs due to phase separation and water condensation**

As a follow-up, we utilized humidity to take advantage of the phase separation observed above. It was assumed that phase separation could be further enhanced if spin-coating was performed under humid conditions. It was further concluded that water condensation would eventually lead to ruptures in the solution layer. By this, a new interface between the solution, water, and SiO_2 substrate would be created. This would induce separation between segregated phases. The condensing water forces the liquid film to dewet and retreat from SiO_2. The viscosity gradient between different phases would lead to the formation of convection cells and honeycomb morphology.(65,66) It was assumed that the spinodal-like structures found during the FS investigation, probably consisting of a higher molecular weight fraction, would reinforce the honeycomb borders. As revealed by the viscosity investigation, the longer polymer chains

20

360 would carry the stress as they would be highly entangled. The lower molecular phase would

361 separate because no stress would be applied to the shorter chains. It should also be considered

362 that MEK is a hygroscopic solvent, while PS is slightly hydrophobic. The absorption of water

363 by MEK can further alter the interactions between the solvent and different PS phases. The

364 viscosity and solubility investigations pointed to 80 mg/ml concentration to obtain the most

365 pronounced effect. It was also assumed that water condensation would take place in the later

366 stage of spinning. As the humidity slows evaporation, the highest humidity allows the longest

367 time for morphology formation. The tested relative humidity Rh values were 45%, 55%, and

368 75%.

369 Fig. 11 A shows images of coatings composed of uniform polystyrenes, Fig. 11 B presents

370 images of coatings prepared from 91 kDa and 200 kDa blends, and Fig. 11 C presents images

371 of coatings prepared from 20 kDa and 200 kDa blends.

372 Each column is marked below with the mixture's PDI value, and each row corresponds to one

373 of the Rh values. Optical microscopy showing three different areas of the coatings is presented

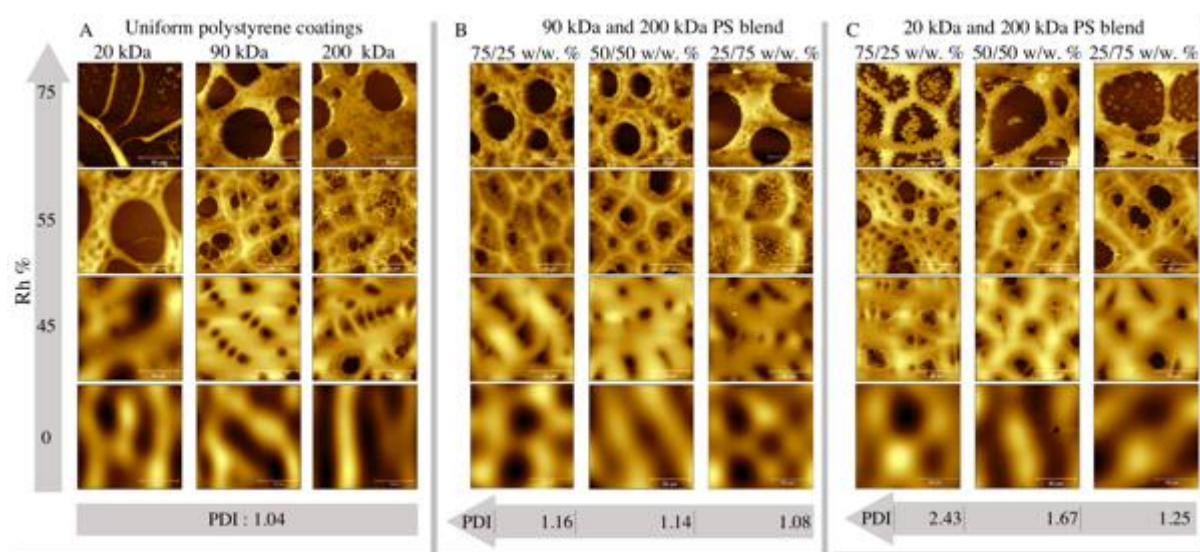374 in the Supplementary Information, Figs. S6 – S8.

375

376

377 Fig. 11 AFM topographical images of tested samples. The colour represents the height, and

378 brighter means higher. The solution concentration C was 80 mg/ml, while the samples were

379 spun under different humidity, from 0 to 75% Rh. The z-scale was chosen for the best

380 representation of the coating morphology. A – uniform coatings; B – 20 kDa and 200 kDa

381 blends; C – 91 kDa and 200 kDa blends. (PowerPoint 365, Gwyddion v2.50,

382 http://gwyddion.net)

383

384 We observed that smaller cavities (breath figures) formed around the larger cavities caused by

385 dewetting-related polymeric film ruptures. The structure that resembles the honeycomb also

386 occurred. For Rh 55%, a honeycomb-like morphology is found for all coatings, except the

387 uniform 20 kDa coating. It is difficult to distinguish uniform samples from the 90 kDa 200 kDa

388 blend. However, the 20 kDa and 200 kDa blends have distinctive morphology that depends on

389 the PDI value. Radially averaged power spectral density analysis (SI, Fig. S9) of four averaged

390 images depicts the differences between the 75/25, 50/50, and 25/75 w/w% 20 kDa and 200 kDa

391 coatings.

392 Interestingly, the coatings prepared from 20 kDa and 200 kDa bimodal blends at Rh 75% had

393 polymeric islands inside the large holes. The onset of such structures can also be observed in

394 the case of coatings prepared in Rh 55%. The fraction of the islands decreased with an increase

395 in the 200 kDa contribution. It was assumed that the islands are made of a lighter and less

396 viscous fraction. Seemingly, the heavier polymer fraction, more viscous and more entangled,

397 reinforced the honeycomb cell borders. The possible scenario is illustrated in Fig. 12. The

398 coatings at Rh 0%, 45%, 55%, and 75% are marked by numbers 1, 2, 3, and 4, respectively. It

399 is assumed that MEK did not evaporate entirely and formed MEK/20 kDa and MEK/200 kDa

400 fractions. It should be noted that MEK is also soluble in water. Thus, some fraction of the

401 solvent can diffuse to the water phase. The MEK/20 kDa fraction becomes dispersed in the

water area of the sample. The MEK/200kDa fraction forms the walls of the cells. Two explanations can be proposed. First, as shown above, the rheological properties of 200 kDa and 20 kDa polystyrene species differ. The more entangled 200 kDa chains act together, while the 20 kDa chains separate from the high-tension region (higher molecular weight) towards the water/MEK interface. However, water has very high polarity. Very nonpolar polystyrene forms a round shape in contact. Furthermore, as was demonstrated, the solvent would deplete the 20 kDa fraction faster than the 200 kDa fraction, allowing for faster solidification of the 20 kDa islands.
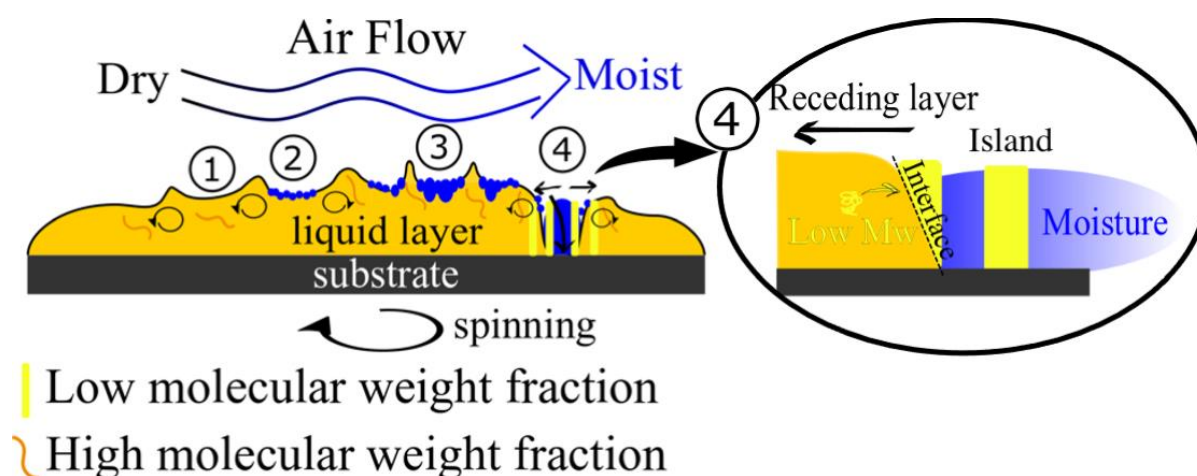
Fig. 12. Four scenarios of phase separation: spin-coating in dry air ((1), 0% Rh); moderate humidity ((2), 45% Rh; (3), 55% Rh); and high humidity ((4), 75% Rh). Low and high molecular weight fractions, convective flow driving honeycomb formation, and low molecular weight separation at the interface between the water-wetted rupture and the liquid layer of the polymer solution are presented. (Inkscape v0.92, https://inkscape.org;)

Second, it can be discussed in terms of the two-step phase separation process discussed by Henderson et al. Their study focused on modelling the two-step quench scenario. First, the solution undergoes a temperature quench into the spinodal decomposition region. After a specific time, a secondary quench was enacted by a further decrease in the temperature. As a

422 result, secondary domains appeared inside the already formed structures.(34) The morphology

423 discussed was very similar to that discussed in the current paper. The presented power spectra

424 of the optical images of the 75/25 w/w% 20 kDa and 200 kDa coatings presented in Fig. 13A

425 coincide with the results presented in the abovementioned paper. Nevertheless, in the current

426 experiment, the first temperature quench is followed by the condensation of water. A decrease

427 in temperature may facilitate the phase separation of polystyrene. Conversely, condensation

428 should coincide with an increase in temperature. (23) However, water may be absorbed by

429 MEK. The MEK/water composition would be a much poorer solvent for PS. Thus, secondary

430 quenching would occur due to the change in solvent quality by water.

431 Fig. 13 presents the characteristic values describing the shape of the islands, Fig. 13 B – height

432 H, Fig. 13 C - radius R, Fig. 13 D - aspect ratio H/R and Fig. 13 E – profile of an island. The

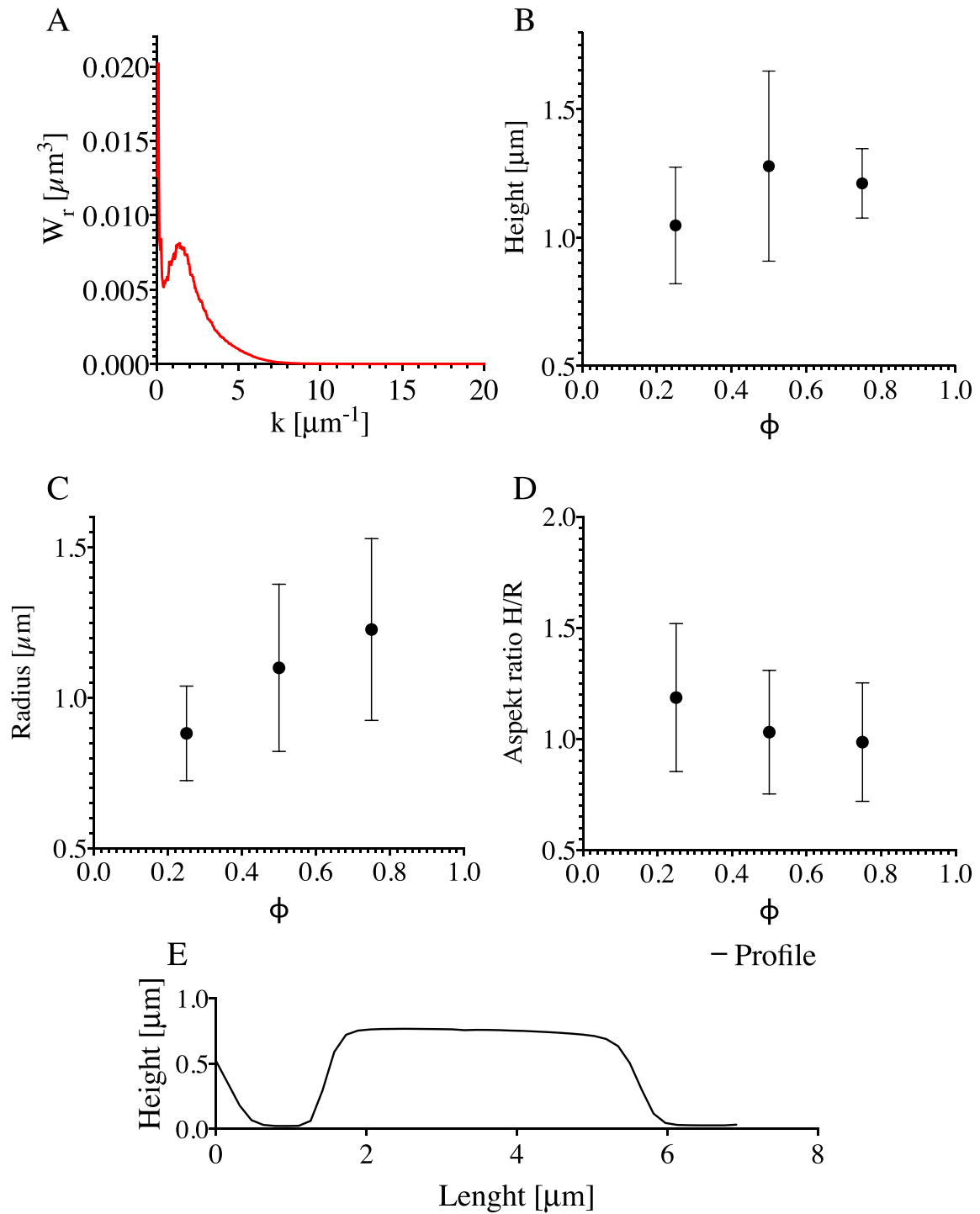433 dependence of the shape on the fraction of 20 kDa PS can be pointed out.

434

Fig. 13. A – Power spectra of islands/honeycomb morphology. B – Mean height, H, of islands with respect to the fraction of 20 kDa PS, ɸ. C – Mean radius of islands, R. D – mean aspect ratio of islands, H/R. H profile of an island. (GraphPad Prism 9, https://www.graphpad.com)

438

Additionally, we tested the formation of micro islands when a short spin-coating time was used (0.5 s and 1 s). These images are presented in Fig. S15 in SI. Secondary phase separation has already been seen, although the islands were not fully formed.

The AFM image (Fig. 14 a-c) shows the event of the low molecular weight fraction separating from the cell border. Cracks between the two phases and the spot where the partially formed island disconnects from the bulk can be seen. The black rectangle indicates the area that differed in terms of the deflection signal and phase contrast. However, the discussed phenomenon appears after the thin film of the solution was formed on the substrate. The condensation required time to make holes in the films. The dewetting of the substrate by the solution can induce additional motion of molecules, allowing the lower molecular weight fraction to precipitate. Water would also change the surface tension locally and induce the thermocapillary effects that lead to the formation of convection cells (depicted in Fig 14 d).
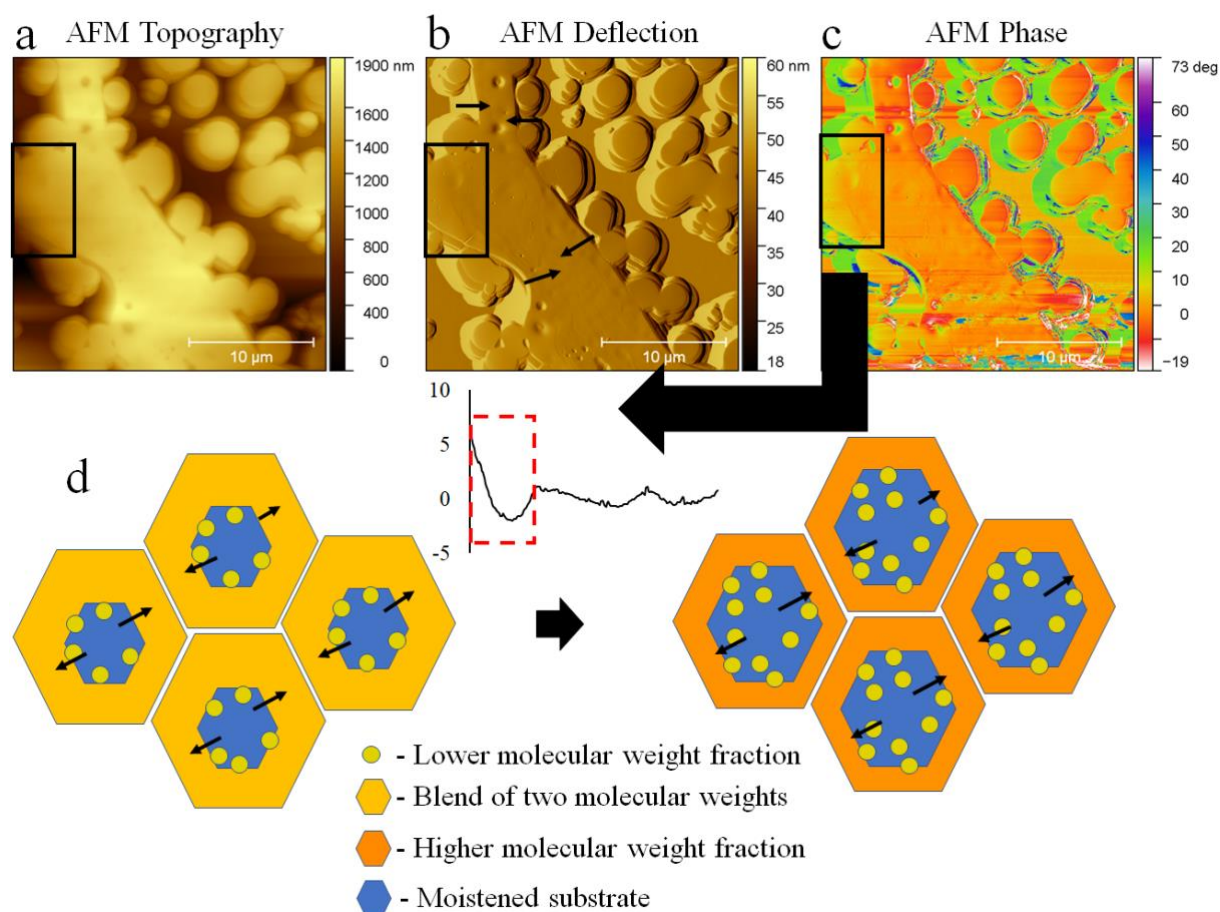
Fig. 14. AFM magnification of the cell border of the 20 kDa and 200 kDa 75/25 w/w% blend spun at Rh 75%. The black rectangle indicates the separation of different phases. The same region is shown in the form of a - topography, b - AFM deflection, the direction of dewetting is indicated by the black arrows; c - AFM phase image, an arrow indicates the phase signal difference presented as the averaged cross-section of the marked region (black box); d – schematic illustration depicting proposed formation mechanism of the honeycomb; Convection inside the liquid film led to cells formation, condensation of water led to film rupture (Blue). Subsequently, the recess of the film occurred. At the interface between the rupture area and the receding film, separation of the lower molecular fraction arises (yellow). Subsequently, the cell borders were reinforced by the remaining high molecular weight fraction (Orange); (PowerPoint 367; Inkscape v0.92, https://inkscape.org; Gwyddion v2.50, http://gwyddion.net)

465   As mentioned, the polystyrenes used were unmodified standard grade polymers. The unchanged

466   chemical composition of the coatings was confirmed by FTIR spectroscopy (SI Fig. S10 – S12).

467   The recognized functional groups were CH_3, CH_2, and phenyl groups. These groups are

468   hydrophobic and were the driving force behind the dewetting process under high humidity

469   conditions. This argument was further reinforced by the free surface energy (SEF) measurement

470   (SI Figs. S13 – S14). The SEF of the 20 kDa coating was slightly higher than that of the 200

471   kDa coating and, consequently, led to a higher affinity for the hydrophilic SiO_2 substrate of the

472   former coating.

473

474   **Conclusions**

475   To the best of our knowledge, we have demonstrated for the first time phase separation in a

476   solution of polystyrenes with identical chemical structures but different molecular weights.

477   Phase separation was found for 90 kDa and 200 kDa blends and 20 kDa and 200 kDa blends.

478   In both cases, phase separation was found for 75/25 and 50/50 w/w%. Force spectroscopy was

479   used to determine the different phases in the coatings. Phase separation was discussed in terms

480   of the difference in the viscosity of polystyrene species. Next, we provoked secondary phase

481   separation by introducing water vapor. We have theorized that water vapor would act two-fold.

482   The water droplets formed breath figures, and as the vapor concentration increased, they caused

483   raptures in the liquid film. Second, the absorption of vapor by methyl ethyl ketone, a solvent

484   chosen due to its hygroscopic properties, would decrease the solubility of polystyrene. We

485   observed secondary phase separation for the 20 kDa and 200 kDa blends. But not for 90 kDa

486   and 200 kDa blends. We also pointed out that the internal thermocapillary convection and

487   gradient of the surface tension of the top layer formed convection cells inside the liquid. The

488   raptures caused by condensation, with the combination of convection and thermocapillary

effects, formed honeycombs. The secondary phase separation left the dispersed 20 kDa polystyrene phase inside the 200 kDa polystyrene honeycomb.

The described mechanism can likely be applied to other solvent-polymer systems, consisting even of three polymer fractions. It is likely possible to apply the described process to other coating methods, such as dip coating, blade coating or ink-jet printing.

Experimental

- **Materials**

All polymers and solvents were purchased from Sigma Aldrich (Merck KGaA). A one-side polished ultrasmooth SiOx wafer was purchased from Technolutions Sp. z o. o.

- **Preparation of the coatings**

Analytical standard grade polystyrenes (PS) obtained from the supplier with PDI = 1.04 and M_w = 20 kDa, 91 kDa, 150 kDa, or 200 kDa were used.

Two kinds of blends were prepared: blends of 20 kDa and 200 kDa PS mixed in 75/25, 50/50, 25/75 w/w % proportions; similarly, blends of 91 kDa and 200 kDa PS were mixed in the same proportions and dissolved in methyl ethyl ketone (analytic grade, MEK) and mixed for an hour at 37 °C. After mixing, the solutions were stored overnight. The list of polystyrene blends used is summarized in Table 1. The concentrations of these solutions ranged from 2.5 mg/ml to 80 mg/ml. A DIY Arduino-based spin-coater with a chamber with controlled humidity was used to spin polystyrene films onto the SiOx wafers. The experimental setup is depicted in Supplementary Information (SI) Figs. S1 – S2. A 35 μl aliquot of the solution was pipetted onto a 1 cm x 1 cm wafer. Spin-coating was performed in a closed chamber with a constant airflow of 10 ml/min to maintain the desired humidity. The rotational speed was 2700 rpm or 3300 rpm.

513 The spinning time was set to 10 s to allow the solvent to evaporate. Solutions were spin-coated

514 under humidity of Rh 0%, 45%, 55%, 75%.

515

516 Table 1. List of polymer blends that were used for spin-coating.

Type of Blend	Sample code	Molecular weight M_w [kDa]		PDI
Uniform	20 kDa	20		1.04
	91 kDa	91		1.04
	150 kDa	150		1.04
	200 kDa	200		1.04
Bimodal	Sample code	Molecular weight		PDI
		$[M_w]$ [kDa] [(1]	$[M_n]$ [kDa] [(2]	
91 kDa / 200 kDa	75/25*	137	118	1.16
	50/50*	166	146	1.14
	25/75*	186	173	1.08
20 kDa / 200 kDa	75/25**	158	65	2.43
	50/50**	184	110	1.67
	25/75**	194	155	1.25

517 *([1]Weight average molecular weight $[M_w] = (f_1 M_{w1}^2 + f_2 M_{w2}^2)/(f_1 M_{w1} + f_2 M_{w2})$, ([2]Number average molecular*

518 *weight $[M_n] = f_1 M_{w1} + f_2 M_{w2}$, where f - fraction of one of the polymers in %; PDI states for the polydispersity*

519 *index.*

520

521   • **Gel permeation chromatography (GPC)**

522 The number and weight average molecular weights (M_n and M_w) were determined by an Agilent

523 1200 series GPC modular system with a refractive index detector (RID) equipped with two

524 PLgel 5 µm MIXED-C columns (300x7.5 mm) in the series, while the polydispersity index was

525 calculated as the ratio of M_w/M_n. Calibration was performed using a set of 12 narrowly

526 distributed polystyrene standards with molecular weights (Mps) in the range of 474 g/mol - 1

527 800 000 g/mol.

528 The measurements were performed at 35 °C. Chloroform GPC grade was used as a solvent at

529 a flow rate of 0.7 ml/min. All samples (~2 mg/ml) were filtered through a PTFE 0.2 µm

530   membrane before the analysis. The data were collected by ChemStation for LC and analysed

531   by ChemStation GPC Data Analysis Software.

532

533   • **Force Spectroscopy FS and Elastic Modulus**

534   When a force spectroscopy experiment is performed, an AFM probe applies strain on the film

535   surface.(67) Force spectroscopy was performed by means of atomic force microscopy (AFM,

536   Asylum Research MFP3D Bio). (68) An OMLCT-AC200TS-R3 (Olympus) cantilever was

537   used with the nominal spring constant k = 9 N/m and tip radius below 10 nm, as suggested by

538   the cantilever's producer. AFM was calibrated using the built-in thermal vibrations method.

539   The (69) Johnson, Kendall, and Roberts (JKR) model was used to calculate the elastic modulus

540   (E).(70) The indentation depth was ~8 nm (Supplementary Information, *4. Force*

541   *Spectroscopy*). As we wanted to neglect the possible influence of stiff (silica) substrate on the

542   polystyrene coating's registered mechanical data, we decided to perform an FS experiment

543   using the thickest films (films spun from the solution of a concentration of 80 mg/ml).

544   Maps of a large area of the coating 80 μm x 80 μm with 40 x 40 points were obtained. These

545   higher resolution maps are supplemented as an attachment (SI). These data were supported by

546   lower resolution maps with a resolution of 15 x 15 points. Each map was used to obtain the

547   mean elastic modulus value. Altogether, at least five maps were made. Ordinary one-way

548   ANOVA followed by multiple comparisons Fisher's test was used to compare different groups'

549   means.

550   Furthermore, histograms representing each higher resolution map were prepared. The skewness

551   of the elastic modulus distribution was measured. Skewness was divided into two groups: one

552   for uniform coatings and one for bimodal coatings. The t-test ($p < 0.05$) was used to compare

553   the means of these two groups.

554

555   • **Evaluation of the thickness of spin-coated films by means of atomic force**

556   **microscopy**

557 The thickness of spin-coated films was assessed based on intentionally made scratch

558 topography images (SI Fig. S3). Five randomly selected areas of each sample were tested, and

559 profiles were generated. Each of the profile lines was averaged from three contiguous lines to

560 avoid any unwanted artefacts.

561

562   • **Imaging of the coatings**

563 Inverted light microscopes (Nikon EPIPHOT 200 and Zeiss Axio Observer) were used for

564 imaging. An atomic force microscope (AFM, Asylum Research MFP3D Bio) working in

565 tapping mode (AC mode) was used to illustrate the phase composition and topography of the

566 polystyrene films.

567

568   • **In situ measurement of evaporation during spin-coating through laser light**

569   **reflectometry with stroboscopic effect**

570 In situ stroboscopic laser light reflectometry was developed to investigate the thinning of the

571 solution layer while spinning. The laser light is reflected from the coating during the spin-

572 coating process. The occurring interference pattern can be used to estimate the thinning rate of

573 the solution. (71–73) The experimental setup is described in SI, Figs. S1 – S2.

574 Depending on the thickness of the layer, constructive or destructive interference can occur. The

575 condition for the constructive interference was calculated from Bragg's law: $2n\Delta h cos\theta = m\lambda$,

576 where n is the refractive index of the layer, Δh is the thickness of the layer, θ is the incident

577 angle, m is an integer number, and λ is the light wavelength. For pure MEK, $\Delta h = 235$ nm

578 (assuming the refractive index MEK = 1.3788). For the polymer solution, it was assumed that

579 the refractive index was $n = 1.5$; thus, $\Delta h = 217$ nm. The laser light wavelength was $\lambda = 650$

580 nm. The time resolution was 0.022 s.

581

582 • **Data analysis and visualisation**

583 For data visualization and analysis: Microsoft PowerPoint 365, Inkscape v0.92, and GraphPad

584 Prism was used. Image analysis procedures implemented in Gwyddion software (ver 2.50) and

585 Igor Pro 6.37 with Asylum Research 15.02.105 add-on were used. Spectragryph v1.5.15 was

586 used for FTIR analysis.

587

588 • **Fourier Transform IR**

589 Infrared spectra were collected using a Fourier transform infrared spectrophotometer (Nicolet

590 8700 FTIR, Thermo Scientific). Measurements were performed using FTIR ATR over a range

591 of 4000−400 cm−1.

592

593 • **Contact Angle and Surface Free Energy Measurement**

594 The contact angle (CA) was measured using a Data Physics OCA 20 goniometer. The contact

595 angle was measured with a sessile drop method. For surface free energy measurement (SFE),

596 two kinds of coatings were chosen: 20 kDa and 200 kDa. For each type of coating, three droplets

597 were measured, and three different coatings were used. Two liquid systems were used:

598 deionised water and diiodomethane (Sigma Aldrich, Analytic grade). The groups were

599 compared with the t-test ($p < 0.05$). The Owens, Wendt, Rabel, and Kaelble (OWKR) method

600 was used for SFE calculation. (74)

601

602 **Supporting Information (SI)**

603 Experimental setup depicting the custom-built spin-coater with a humidity-controlled chamber

604 and an in situ interferometer with the stroboscopic effect. Illustration of thickness measurement.

605 Viscosity-related coefficients. Optical microscope images. FTIR results. Free Surface Energy

606 results.

607

608 **Author information**

609 Corresponding authors:

610 Maciej Łojkowski, ORCID: 0000-0002-0612-7964, email: 00183042@pw.edu.pl

611 Wojciech Swieszkowski, ORCID: 0000-0003-4216-9974, email:

612 wojciech.swieszkowski@pw.edu.pl.

613

614 The authors declare no competing financial interest.

615

616 **Acknowledgements**

621

622 **Authors contributions:**

623 Conceptualization, M.Ł. ; methodology, M.Ł., A.Ch., E.Ch. ; investigation, M.Ł., A.Ch., E.

624 Ch., imaging, M.Ł., A.Ch. ; data analysis, M.Ł. ; visualisation, M.Ł. ; writing, M.Ł. ;

625 supervision, W. Ś.; revision of the manuscript, M.Ł., A.Ch., E. Ch., W. Ś; funding acquisition

626 W. Ś. All authors have read and agreed to the published version of the manuscript.

627

Abbreviations

AFM – atomic force microscopy; bimodal – polymer with two nodes in molecular weight distribution; coating – final polymer coating; CA – contact angle; E – elastic modulus; film – liquid film of solution spread on the substrate; FS – force spectroscopy; FTIR – Fourier transform IR; GPC – gel permeation chromatography; initial solution – solution at the start of spin-coating; MEK – methyl ethyl ketone; Mw – molecular weight; $[M_w]$ – weight average molecular weight; $[M_n]$ – number average molecular weight; MWD – molecular weight distribution; PDI – polydispersity index; PTF – polymer thin film; PS – polystyrene; Rh% - relative humidity in %; RMS – root mean square roughness; uniform – polymer with one node in molecular weight distribution.

References

1. Kumar M, Bhardwaj R. Wetting characteristics of Colocasia esculenta (Taro) leaf and a bioinspired surface thereof. Sci Rep. 2020;10(1):1–15.

2. He R, Xiao J, Zhang M, Zhang Z, Zhang W, Cao Y, et al. Artificial honeycomb-inspired TiO2 nanorod arrays with tunable nano/micro interfaces for improving poly(dimethylsiloxane) surface hydrophobicity. J Mater Sci. 2016;51(6):2935–41.

3. Jahed Z, Shahsavan H, Verma MS, Rogowski JL, Seo BB, Zhao B, et al. Bacterial Networks on Hydrophobic Micropillars. ACS Nano. 2017;11(1):675–83.

4. Liu X, Liu R, Cao B, Ye K, Li S, Gu Y, et al. Subcellular cell geometry on micropillars regulates stem cell differentiation. Biomaterials [Internet]. 2016 Dec;111:27–39. Available from: http://dx.doi.org/10.1016/j.biomaterials.2016.09.023

5. Walheim S, Böltau M, Mlynek J, Krausch G, Steiner U. Structure Formation via Polymer Demixing in Spin-Cast Films. Macromolecules [Internet]. 1997 Aug 1;30(17):4995–5003. Available from: https://doi.org/10.1021/ma9619288

653   6.   Daly R, Sader JE, Boland JJ. The dominant role of the solvent–water interface in water

654   droplet templating of polymers. Soft Matter [Internet]. 2013;9(33):7960. Available

655   from: http://xlink.rsc.org/?DOI=c3sm51452h

656   7.   Khikhlovskyi V, Wang R, van Breemen AJJM, Gelinck GH, Janssen RAJ, Kemerink

657   M. Nanoscale Organic Ferroelectric Resistive Switches. J Phys Chem C [Internet].

658   2014 Feb 13;118(6):3305–12. Available from:

659   https://pubs.acs.org/doi/10.1021/jp409757m

660   8.   D'Andrade BW, Forrest SR. White Organic Light-Emitting Devices for Solid-State

661   Lighting. Adv Mater [Internet]. 2004 Sep 16;16(18):1585–95. Available from:

662   http://doi.wiley.com/10.1002/adma.200400684

663   9.   Yabu H. Fabrication of honeycomb films by the breath figure technique and their

664   applications. Sci Technol Adv Mater [Internet]. 2018;19(1):802–22. Available from:

665   https://doi.org/10.1080/14686996.2018.1528478

666   10.   Wu D, Xu F, Sun B, Fu R, He H, Matyjaszewski K. Design and Preparation of Porous

667   Polymers. Chem Rev [Internet]. 2012 Jul 11;112(7):3959–4015. Available from:

668   https://pubs.acs.org/doi/10.1021/cr200440z

669   11.   Karagkiozaki V, Vavoulidis E, Karagiannidis PG, Gioti M, Fatouros DG, Vizirianakis

670   IS, et al. Development of a nanoporous and multilayer drug-delivery platform for

671   medical implants. Int J Nanomedicine. 2012;7(October):5327–38.

672   12.   Calejo MT, Ilmarinen T, Skottman H, Kellomäki M. Breath figures in tissue

673   engineering and drug delivery: State-of-the-art and future perspectives. Vol. 66, Acta

674   Biomaterialia. 2018.

675   13.   Vendra VK, Wu L, Krishnan S. Polymer Thin Films for Biomedical Applications. In:

676   Nanotechnologies for the Life Sciences [Internet]. Weinheim, Germany: Wiley-VCH

677   Verlag GmbH & Co. KGaA; 2011. Available from:

678   http://doi.wiley.com/10.1002/9783527610419.ntls0179

679   14.   Griesser HJ. Thin Film Coatings for Biomaterials and Biomedical Applications, 1st

680   Edition. 2016. 310 p.

681   15.   Łojkowski M, Walheim S, Jokubauskas P, Schimmel T, Święszkowski W. Tuning the

682   wettability of a thin polymer film by gradually changing the geometry of nanoscale

683   pore edges. Langmuir [Internet]. 2019;35(17):5987–96. Available from:

684   https://doi.org/10.1021/acs.langmuir.9b00467

685   16.   Plawsky JL, Kim JK, Schubert EF. Engineered nanoporous and nanostructured films.

686   Mater Today [Internet]. 2009;12(6):36–45. Available from:

687   http://dx.doi.org/10.1016/S1369-7021(09)70179-8

688   17.   Bormashenko E. Breath-figure self-assembly, a versatile method of manufacturing

689   membranes and porous structures: Physical, chemical and technological aspects.

690   Membranes (Basel). 2017;7(3).

691   18.   Birnie DP. Rational solvent selection strategies to combat striation formation during

692   spin coating of thin films. J Mater Res. 2001;16(4):1145–54.

693   19.   van Franeker JJ, Westhoff D, Turbiez M, Wienk MM, Schmidt V, Janssen RAJ.

694   Controlling the Dominant Length Scale of Liquid-Liquid Phase Separation in Spin-

695   coated Organic Semiconductor Films. Adv Funct Mater [Internet]. 2015

696   Feb;25(6):855–63. Available from: http://doi.wiley.com/10.1002/adfm.201403392

697   20.   Schaefer C, Michels JJ, van der Schoot P. Structuring of Thin-Film Polymer Mixtures

698   upon Solvent Evaporation. Macromolecules [Internet]. 2016 Sep 27;49(18):6858–70.

699   Available from: https://pubs.acs.org/doi/10.1021/acs.macromol.6b00537

700   21.   Ebbens S, Hodgkinson R, Parnell AJ, Dunbar A, Martin SJ, Topham PD, et al. In Situ

701   Imaging and Height Reconstruction of Phase Separation Processes in Polymer Blends

702   during Spin Coating. ACS Nano [Internet]. 2011 Jun 28;5(6):5124–31. Available from:

703 https://pubs.acs.org/doi/10.1021/nn201210e

704 22. Danglad-Flores J, Eickelmann S, Riegler H. Deposition of polymer films by spin

705 casting: A quantitative analysis. Chem Eng Sci [Internet]. 2018 Apr;179:257–64.

706 Available from: https://linkinghub.elsevier.com/retrieve/pii/S0009250918300125

707 23. Dombrovsky LA, Frenkel M, Legchenkova I, Bormashenko E. Effect of thermal

708 properties of a substrate on formation of self-arranged surface structures on evaporated

709 polymer films. Int J Heat Mass Transf [Internet]. 2020;158:120053. Available from:

710 https://doi.org/10.1016/j.ijheatmasstransfer.2020.120053

711 24. Daly R, Sader JE, Boland JJ. Taming Self-Organization Dynamics to Dramatically

712 Control Porous Architectures. ACS Nano [Internet]. 2016 Mar 22;10(3):3087–92.

713 Available from: https://pubs.acs.org/doi/10.1021/acsnano.5b06082

714 25. Zabusky HH, Heitmiller RF. Properties of high density polyethylenes with bimodal

715 molecular weight distribution. Polym Eng Sci. 1964;4(1):17–21.

716 26. Wu BH, Zhong QZ, Xu ZK, Wan LS. Effects of molecular weight distribution on the

717 self-assembly of end-functionalized polystyrenes. Polym Chem. 2017;8(29):4290–8.

718 27. Jiang H, Zhang L, Qin J, Zhang W, Cheng Z, Zhu X. Producing bimodal molecular

719 weight distribution polymers through facile one-pot/one-step RAFT polymerization. J

720 Polym Sci Part A Polym Chem. 2012;50(19):4103–9.

721 28. Whitfield R, Parkatzidis K, Truong NP, Junkers T, Anastasaki A. Tailoring Polymer

722 Dispersity by RAFT Polymerization: A Versatile Approach. Chem [Internet]. 2020

723 Jun;6(6):1340–52. Available from:

724 https://linkinghub.elsevier.com/retrieve/pii/S2451929420301923

725 29. Tanaka K, Takahara A, Kajiyama T. Effect of Polydispersity on Surface Molecular

726 Motion of Polystyrene Films. Macromolecules [Internet]. 1997 Oct;30(21):6626–32.

727 Available from: https://pubs.acs.org/doi/10.1021/ma970057e

728   30.   Heitmiller RF, Naar RZ, Zabusky HH. Effect of homogeneity on viscosity in capillary

729   extrusion of polyethylene. J Appl Polym Sci [Internet]. 1964 Mar;8(2):873–80.

730   Available from: http://doi.wiley.com/10.1002/app.1964.070080226

731   31.   Koningsveld R, Chermin HAG, Gordon M. Liquid─liquid phase separation in

732   multicomponent polymer solutions - VIII. Stability limits and consolute states in quasi-

733   ternary mixtures. Proc R Soc London A Math Phys Sci [Internet]. 1970 Oct

734   27;319(1538):331–49. Available from:

735   https://royalsocietypublishing.org/doi/10.1098/rspa.1970.0182

736   32.   Zeman L, Patterson D. Effect of the Solvent on Polymer Incompatibility in Solution.

737   Macromolecules [Internet]. 1972 Jul;5(4):513–6. Available from:

738   https://pubs.acs.org/doi/abs/10.1021/ma60028a030

739   33.   Shultz AR, Flory PJ. Phase Equilibria in Polymer—Solvent Systems1,2. J Am Chem

740   Soc [Internet]. 1952 Oct 1;74(19):4760–7. Available from:

741   https://doi.org/10.1021/ja01139a010

742   34.   Henderson IC, Clarke N. Two-Step Phase Separation in Polymer Blends.

743   Macromolecules. 2004;37(5):1952–9.

744   35.   Tanaka H. Viscoelastic phase separation in soft matter and foods. Faraday Discuss.

745   2012;158:371–406.

746   36.   Hengeller L, Huang Q, Dorokhin A, Alvarez NJ, Almdal K, Hassager O. Stress

747   relaxation of bi-disperse polystyrene melts: Exploring the interactions between long

748   and short chains in non-linear rheology. Rheol Acta. 2016;55(4):303–14.

749   37.   Harris EK. Effect of blending on the rheological properties of polystyrene. J Appl

750   Polym Sci [Internet]. 1973 Jun;17(6):1679–92. Available from:

751   http://doi.wiley.com/10.1002/app.1973.070170604

752   38.   Klein J. The Onset of Entangled Behavior in Semidilute and Concentrated Polymer

753   Solutions. Macromolecules [Internet]. 1978 Sep;11(5):852–8. Available from:

754   https://pubs.acs.org/doi/abs/10.1021/ma60065a002

755 39. Hong KM, Noolandi J. Theory of inhomogeneous multicomponent polymer systems.

756   Macromolecules [Internet]. 1981 May;14(3):727–36. Available from:

757   https://pubs.acs.org/doi/abs/10.1021/ma50004a051

758 40. Hariharan A, Kumar SK, Russell TP. A lattice model for the surface segregation of

759   polymer chains due to molecular weight effects. Macromolecules [Internet]. 1990

760   Jul;23(15):3584–92. Available from:

761   https://pubs.acs.org/doi/abs/10.1021/ma00217a009

762 41. Mahmoudi P, Matsen MW. Entropic segregation of short polymers to the surface of a

763   polydisperse melt. Eur Phys J E [Internet]. 2017 Oct 6;40(10):85. Available from:

764   http://link.springer.com/10.1140/epje/i2017-11575-7

765 42. Hill JA, Endres KJ, Mahmoudi P, Matsen MW, Wesdemiotis C, Foster MD. Detection

766   of Surface Enrichment Driven by Molecular Weight Disparity in Virtually

767   Monodisperse Polymers. ACS Macro Lett [Internet]. 2018 Apr 17;7(4):487–92.

768   Available from: https://pubs.acs.org/doi/10.1021/acsmacrolett.7b00993

769 43. Stein GE, Laws TS, Verduzco R. Tailoring the Attraction of Polymers toward Surfaces.

770   Macromolecules [Internet]. 2019 Jul 9;52(13):4787–802. Available from:

771   https://pubs.acs.org/doi/10.1021/acs.macromol.9b00492

772 44. Carlier V, Sclavons M, Jonas AM, Jérôme R, Legras R. Probing Thermoplastic

773   Matrix−Carbon Fiber Interphases. 1. Preferential Segregation of Low Molar Mass

774   Chains to the Interface. Macromolecules [Internet]. 2001 May;34(11):3725–9.

775   Available from: https://pubs.acs.org/doi/10.1021/ma000404b

776 45. Suwa J, Kakiage M, Yamanobe T, Komoto T, Uehara H. Molecular Weight

777   Segregation on Surfaces of Polyethylene Blended Films as Estimated from

Nanoscratch Tests Using Scanning Probe Microscopy. Langmuir [Internet]. 2007 May;23(11):5882–5. Available from: https://pubs.acs.org/doi/10.1021/la070150o

46.   Karim A, Slawecki TM, Kumar SK, Douglas JF, Satija SK, Han CC, et al. Phase-Separation-Induced Surface Patterns in Thin Polymer Blend Films. Macromolecules [Internet]. 1998 Feb;31(3):857–62. Available from: https://pubs.acs.org/doi/10.1021/ma970687g

47.   Hoppe H, Heuberger M, Klein J. Self-Similarity and Pattern Selection in the Roughening of Binary Liquid Films. Phys Rev Lett [Internet]. 2001 May 21;86(21):4863–6. Available from: https://link.aps.org/doi/10.1103/PhysRevLett.86.4863

48.   Heier J, Kramer EJ, Revesz P, Battistig G, Bates FS. Spinodal Decomposition in a Subsurface Layer of a Polymer Blend Film. Macromolecules [Internet]. 1999 Jun;32(11):3758–65. Available from: https://pubs.acs.org/doi/10.1021/ma981709h

49.   Jandt KD, Heier J, Bates FS, Kramer EJ. Transient surface roughening of thin films of phase separating polymer mixtures. Langmuir. 1996;12(15):3716–20.

50.   Huang C, Förste A, Walheim S, Schimmel T. Polymer blend lithography for metal films: Large-area patterning with over 1 billion holes/inch2. Beilstein J Nanotechnol. 2015;6(1):1205–11.

51.   Flory PJ, Höcker H. Thermodynamics of polystyrene solutions. Part 1.—Polystyrene and methyl ethyl ketone. Trans Faraday Soc [Internet]. 1971;67:2258–69. Available from: http://xlink.rsc.org/?DOI=TF9716702258

52.   Imre A, Van Hook WA. Liquid-liquid demixing from solutions of polystyrene. 1. A review. 2. Improved correlation with solvent properties. Vol. 25, Journal of Physical and Chemical Reference Data. 1996. p. 637–61.

53.   Utracki LA, Wilkie CA. Polymer blends handbook. Polymer Blends Handbook. 2014.

803 1–2378 p.

804 54. Ying Q, Chu B. Overlap concentration of macromolecules in solution. Macromolecules

805 [Internet]. 1987 Mar;20(2):362–6. Available from:

806 https://pubs.acs.org/doi/abs/10.1021/ma00168a023

807 55. Kim JK, Taki K, Nagamine S, Ohshima M. Periodic porous stripe patterning in a

808 polymer blend film induced by phase separation during spin-casting. Langmuir.

809 2008;24(16):8898–903.

810 56. Heier J, Kramer EJ, Groenewold J, Fredrickson GH. Kinetics of individual block

811 copolymer island formation and disappearance near an absorbing boundary.

812 Macromolecules. 2000;33(16):6060–7.

813 57. Coveney S, Clarke N. Pattern formation in polymer blend thin films: Surface

814 roughening couples to phase separation. Phys Rev Lett. 2014;113(21):1–5.

815 58. Mecke K. Additivity, Convexity, and Beyond: Applications of Minkowski Functionals

816 in Statistical Physics. Stat Phys Spat Stat [Internet]. 2000;111–84. Available from:

817 http://link.springer.com/chapter/10.1007/3-540-45043-2_6

818 59. Wolf BA. Improvement of polymer solubility: Influence of shear and of pressure. Pure

819 Appl Chem. 1997;69(5):929–33.

820 60. Du B, Tsui OKC, Zhang Q, He T. Study of Elastic Modulus and Yield Strength of

821 Polymer Thin Films Using Atomic Force Microscopy. Langmuir [Internet]. 2001

822 May;17(11):3286–91. Available from: https://pubs.acs.org/doi/10.1021/la001434a

823 61. Landel RF, Nielsen LE. Mechanical properties of polymers and composites. CRC

824 press; 1993.

825 62. Torres JM, Stafford CM, Vogt BD. Impact of molecular mass on the elastic modulus of

826 thin polystyrene films. Polymer (Guildf) [Internet]. 2010;51(18):4211–7. Available

827 from: http://dx.doi.org/10.1016/j.polymer.2010.07.003

828   63.   Kok CM, Rudin A. Prediction of Flory–Huggins interaction parameters from intrinsic

829   viscosities. J Appl Polym Sci. 1982;27(2):353–62.

830   64.   Lee SH, Lee SB. The Hildebrand solubility parameters, cohesive energy densities and

831   internal energies of 1-alkyl-3-methylimidazolium-based room temperature ionic

832   liquids. Chem Commun. 2005;(27):3469–71.

833   65.   Bormashenko E, Malkin A, Musin A, Bormashenko Y, Whyman G, Litvak N, et al.

834   Mesoscopic patterning in evaporated polymer solutions: Poly(ethylene glycol) and

835   room-temperature-vulcanized polyorganosilanes/-siloxanes promote formation of

836   honeycomb structures. Macromol Chem Phys. 2008;209(6):567–76.

837   66.   Uchiyama H, Matsui T, Kozuka H. Spontaneous Pattern Formation Induced by

838   Bénard–Marangoni Convection for Sol–Gel-Derived Titania Dip-Coating Films: Effect

839   of Co-solvents with a High Surface Tension and Low Volatility. Langmuir [Internet].

840   2015 Nov 17;31(45):12497–504. Available from:

841   https://pubs.acs.org/doi/10.1021/acs.langmuir.5b02929

842   67.   Zgłobicka I, Chlanda A, Woźniak M, Łojkowski M, Szoszkiewicz R, Mazurkiewicz-

843   Pawlicka M, et al. Microstructure and nanomechanical properties of single stalks from

844   diatom Didymosphenia geminata and their change due to adsorption of selected metal

845   ions. J Phycol. 2017;53(4).

846   68.   Chlanda A, Kijeńska-Gawrońska E, Zdunek J, Swieszkowski W. Internal

847   nanocrystalline structure and stiffness alterations of electrospun polycaprolactone-

848   based mats after six months of in vitro degradation. An atomic force microscopy assay.

849   J Mech Behav Biomed Mater [Internet]. 2020 Jan;101(August 2019):103437.

850   Available from: https://linkinghub.elsevier.com/retrieve/pii/S1751616119305156

851   69.   Sader JE, Borgani R, Gibson CT, Haviland DB, Michael J, Kilpatrick JI, et al. A virtual

852   instrument to standardise the calibration of atomic force microscope cantilevers. Rev

853   Sci Instrum [Internet]. 2016 Sep 1;87(9):093711. Available from:

854   http://dx.doi.org/10.1063/1.4962866

855   70.   Wu KC, You HI. Determination of solid material elastic modulus and surface energy

856   based on JKR contact model. Appl Surf Sci. 2007;253(20):8530–7.

857   71.   Toolan DTW. Straightforward technique for in situ imaging of spin-coated thin films .

858   Opt Eng. 2015;54(2):024109.

859   72.   Toolan DTW, Howse JR. Development of in situ studies of spin coated polymer films.

860   J Mater Chem C. 2013;1(4):603–16.

861   73.   Mokarian-Tabari P, Geoghegan M, Howse JR, Heriot SY, Thompson RL, Jones RAL.

862   Quantitative evaluation of evaporation rate during spin-coating of polymer blend films:

863   Control of film structure through defined-atmosphere solvent-casting. Eur Phys J E.

864   2010;33(4):283–9.

865   74.   Drelich JW, Boinovich L, Chibowski E, Volpe C Della, Hołysz L, Marmur A, et al.

866   Contact Angles: History of Over 200 Years of Open Questions. Surf Innov [Internet].

867   2019;(March):1–25. Available from:

868   https://www.icevirtuallibrary.com/doi/10.1680/jsuin.19.00007

869

870   Fig 1. Exemplary GPC experiment results of bimodal and uniform MWD polystyrene; A -

871   narrow uniform MWD, Mw = 91 kDa, PDI 1.04; B – bimodal MWD, blend of Mw = 91 kDa,

872   PDI = 1.04 and Mw = 200 kDa, PDI = 1.04.

873

874   Fig. 2. Reduced viscosity η_r/C of the solutions, A - η_r/C plotted against the solution's

875   concentration. Curves represent fits for eq. 2; B - η_r/C plotted as a function of the number

876   average molecular weight function. Curves represent the Mark-Houwink equation fit (eq. 3),

877   $[M_n] = f_1 M_{w1} + f_2 M_{w2}$, where f is w/w % ratio of polymers.

878

879   Fig. 3. The relation between the evaporation rate of solution and the reduced viscosity of

880   solution for polymer concentrations: A - 20 mg/ml, B - 40 mg/ml, and C - 80 mg/ml. The curves

881   represent the Padé approximation trend line.

882

883   Fig. 4. A - Thickness of the coatings with respect to the composition and the concentration. The

884   plot presents data for uniform and 91 kDa/200 kDa solutions. B – Thickness of the coating for

885   80 mg/ml concentration in the blend's molecular weight function. * - Blends of 91 kDa and 200

886   kDa polystyrene; ** - blend of 20 kDa and 200 kDa polystyrene; x/x – w/w% ratio of blended

887   homogeneous polystyrenes. The number average molecular weight $[M_n] = f_1 M_{w1} + f_2 M_{w2}$,

888   where f w/w. % ratio of polymers. C - RMS roughness of the coatings spun from 80 mg/ml

889   concentration.

890

891   Fig. 5. A - Optical images of coatings spun from 80 mg/ml. The B - Minkowski connectivity

892    $C(\nu)$ of the coatings spun from 80 mg/ml, where ν represents the threshold for image

893   binarization. The values on the axis were normalized to 1.

894

895   Fig. 6. Average elastic modulus obtained based on the FS method for coatings made from a

896   solution of 80 mg/ml. Uniform – coatings were made from homogeneous solutions; bimodal –

897   coatings made from solutions with bimodal MWD; * - blends of 91 kDa and 200 kDa

898   polystyrene; ** - blend of 20 kDa and 200 kDa polystyrene; x/x – w/w% ratio of blended

899   homogeneous polystyrenes. $[M_n] = f_1 M_{w1} + f_2 M_{w2}$, where f w/w % ratio of polymers. *** -

900   means are significantly different (one-way ANOVA, $p < 0.05$).

901

902   Fig. 7. Force spectroscopy maps of bimodal MWD coatings and corresponding histograms of

903   the elastic modulus. The greyscale shows the stiffness – the white colour corresponds to the

904   highest stiffness. The grayscale range is ± 1 GPa.

905

906   Fig. 8. Force spectroscopy maps of coatings with uniform MWD and corresponding histograms

907   of the elastic modulus. The greyscale shows the stiffness – the white colour corresponds to the

908   highest stiffness. The grayscale range is ± 1 GPa.

909

910   Fig 9. The skewness of the elastic modulus data sets. Uniform – grouped means that represents

911   the skewness of histograms of uniform coatings elastic modulus. Bimodal – grouped means that

912   represents the skewness of histograms of all kinds of bimodal blends elastic modulus. The

913   means of these two groups were significantly different ($p < 0.05$).

914

915   Fig. 10. The effective miscibility parameter δ_{eff} of the polystyrenes in MEK with bimodal and

916   uniform distributions for two kinds of bimodal distributions: 20 kDa/200 kDa – brown squares

917   and 91 kDa/200 kDa – purple triangles; the blue circles represent data for polystyrenes with

918   uniform distributions. $[M_n] = f_1 M_{w1} + f_2 M_{w2}$, where f w/w % ratio of polymers.

919

920   Fig. 11 AFM topographical images of tested samples. The colour represents the height, and

921   brighter means higher. The solution concentration C was 80 mg/ml, while the samples were

922   spun under different humidity, from 0 to 75% Rh. The z-scale was chosen for the best

923   representation of the coating morphology. A – uniform coatings; B – 20 kDa and 200 kDa

924   blends; C – 91 kDa and 200 kDa blends.

925

926   Fig. 12. Four scenarios of phase segregation: spin-coating in dry air ((1), 0% Rh); moderate

927   humidity ((2), 45% Rh; (3), 55% Rh); and high humidity ((4), 75% Rh). Low and high

928   molecular weight fractions, convective flow driving honeycomb formation, and low molecular

929   weight separation at the interface between the water-wetted rupture and the liquid layer of the

930   polymer solution are presented.

931

932   Fig. 13. A – Power spectra of islands/honeycomb morphology. B – Mean height, H, of islands

933   with respect to the fraction of 20 kDa PS, ϕ. C – Mean radius of islands, R. D – mean aspect

934   ratio of islands, H/R. H profile of an island.

935

936   Fig. 14. AFM magnification of the cell border of the 20 kDa and 200 kDa 75/25 w/w% blend

937   spun at Rh 75%. The black rectangle indicates the separation of different phases. The same

938   region is shown in the form of a - topography, b - AFM deflection, the direction of dewetting

939   is indicated by the black arrows; c - AFM phase image, an arrow indicates the phase signal

940   difference presented as the averaged cross-section of the marked region (black box); d –

941   schematic illustration depicting proposed formation mechanism of the honeycomb; Convection

942   inside the liquid film led to cells formation, condensation of water led to film rupture (Blue).

943   Subsequently, the recess of the film occurred. At the interface between the rupture area and the

944   receding film, segregation of the lower molecular fraction arises (yellow). Subsequently, the

945   cell borders were reinforced by the remaining high molecular weight fraction (Orange);

946